PCCP

Accepted Manuscript

ROYAL SOCIETY OF CHEMISTRY

www.rsc.org/pccp

Ti/ZnO–M_xO_y composite (M=Al, Cr, Fe, Ce): synthesis, characterization and application as a highly efficient photocatalyst for hexachlorobenzene degradation

Shengjie Xia,[a] Mengmeng Shao,[a] Xiaobo Zhou,[b] Guoxiang Pan,[c] and Zheming Ni [a]*

[a] Department of Chemistry, College of Chemical Engineering, Zhejiang University of Technology, Hangzhou 310032, P R China

[b] Toxikon Corporation, 15 Wiggins Ave, Bedford, Massachusetts 01730, USA

[c] Department of Materials Chemistry, School of Life Science, Huzhou Teachers college, Huzhou 313000, P R China

* Corresponding author.

E–mail: jchx@zjut.edu.cn

Telephone number: 086–0571–88320373

Abstract: A series of novel organic–inorganic nanoscale layered materials were synthesized by intercalating Ti–containing schiff base complex into the interlayer of the ZnM layered double hydroxides (LDHs, M=Al, Cr, Fe, Ce). The hybrid material was further calcined to make metal oxide composites with highly dispersed of Ti element (Ti/ZnO–M_xO_y). The structural characterization and photocatalytic results showed that, after intercalation and calcination, the metal oxide composites with special flower–like crystal morphology not only had high specific surface area, uniform pore size distribution and narrow band gap, but also showed extremely high photocatalytic performance for hexachlorobenzene (HCB) degradation. Ti/ZnO–Cr_2O_3 composite with narrowest bang gap (2.40 eV) and highest surface area (227 m^2) showed highest photocatalytic performance for HCB (95.5% within 240 min) among four metal oxide composites. Particularly, it was found that composites derived from layered materials with different supramolecular structure of the host and guest showed different photocatalytic property. In addition, based on the results from ESR, GC–MS and HPLC–MS, the type and amount of hydroxyl radicals, the decomposition intermediates and pathway for HCB photocatalyzed by Ti/ZnO–M_xO_y composites were also discussed in detail.

Keywords: Zn–based layered double hydroxides, Ti/schiff base complex, Photodegradation, Hexachlorobenzene, Supramolecular structure

1. Introduction

Layered double hydroxides (LDHs) are a class of host–guest layered solids with the general formula $[M^{2+}_{1-x}M^{3+}_{x}(OH)_2]^{x+}A^{n-}_{x/n}\cdot mH_2O$, where M^{2+} and M^{3+} are di– and trivalent metal cations, respectively; A^{n-} denotes exchangeable inorganic or organic anions with negative charge n, m is the number of interlayer water molecule and x ($=\frac{M^{3+}}{M^{2+}+M^{3+}}$) is the layer charge density of LDHs [1–3]. LDHs is a group of layered functional materials with special octahedral micro–structure, it has the following major features: (1) the chemical composition of the layers is adjustable, (2) the type and amount of the interlayer anions are changeable, (3) controllable particle size and particle size distribution [4–6]. When Mg and Al element of the traditional MgAl–LDHs are replaced by Zn or Fe, particularly for Ti, it could narrow the band gap of the new LDHs would be narrowed [7–9]. The narrowing of band gap would improve the photocatalytic oxidation–reduction activity of the material because the valence electrons could be exited into the conduction state and creates electron–hole pair more easily. In addition, researchers have found that after calcination at high temperature, multi–metal oxides structure could be produced, it retained the original O–M–O (M: metal elements) and at the same time the introduced new metal element could be doped in the layer structure with high dispersion. The calcination brought in narrow band gap, high specific area and uniform pore size distribution, which could also increase the photocatalytic activity [10,11]. Also, studies have shown that when LDH material was modified with organic complexes or other metal oxides (CeO_2,

Cr_2O_3, Fe_2O_3, and so on) with good photocatalytic activity, the surface properties could be changed and the photo activity could be further improved [12].

Currently, the study of the LDHs or metal oxides derived from LDHs used as photocatalysts has been focused on the application of traditional Mg and Zn–containing LDH–based materials for organic pollutant compound degradation reaction [13–15]. And photocatalytic objects were always traditional organic pollutants, such as azo dyes, which were relatively easier to decomposed [16,17]. While, due to the property of high chromaticity, complex molecular structure, high chemical stability and low biodegradability, chlorobenzene compounds were very hard to degrade [18,19]. At present, a few researchers have paid attention to the photodecomposition of chlorobenzene compounds, but the catalysts used in these works were focus on traditional molecular sieve or TiO_2 materials with doping or surface modification. And the photocatalytic efficiency was not very high [20–23]. Based on our study, very little progress has been made on the study of metal oxides derived from LDHs for chlorobenzene degradation. And our former works showed that the photocatalytic performance could be improved after the intercalation of organic ligands contained Ti element into LDHs interlayer [24]. In addition, no research has been reported so far on the idea of designing a novel metal oxide composites based on Ti–containing organic–inorganic hybrid material and applying this new material into the researching field of chlorobenzene photo oxidation.

Based on the above–mentioned research idea, in this paper, we introduced Al, Cr, Fe and Ce elements into the layers to synthesize the ZnM–LDHs (M=Al, Cr, Fe, Ce),

followed by introducing the Ti–containing schiff–base complex into the LDH interlayer by ion exchange method, the prepared layered hybrid LDH materials were further calcined at high temperature to obtain the final composites of metal oxides contained Zn, Ti and other elements. The photocatalytic performance for hexachlorobenzene degradation by these composites was further studied in detail. Moreover, we also investigated the microstructure and physicochemical property of the composite, as well as the catalysts' regeneration, the reaction mechanism and intermediates for hexachlorobenzene decomposition under visible light.

2. Experimental Section

2.1. Materials.

Hexachlorobenzene (abbreviated as HCB here), sodium 4–aminobenzoate and salicylaldehyde were guaranteed reagent (GR) and purchased from Aldrich. Titanium tetrachloride, diethyl ether and formic acid were analytical reagent (AR) and purchased from Aladdin Chemistry Co. Ltd. The others were all purchased from Zhejiang Xiaoshan Fine Chemical Co. Ltd. In addition, deionized water was decarbonated by boiling N_2 before employing in all synthesis process.

2.2. Synthesis of ZnAl–LDHs, ZnCr–LDHs and ZnFe–LDHs.

A typical synthetic procedure is given below: under N_2 atmosphere, an aqueous solution (100 mL) containing 20.0 g NaOH (0.50 mol) was added dropwise to a solution (150 mL) containing 44.6 g (0.15 mol) of $Zn(NO_3)_2 \cdot 6H_2O$ and 18.8 g $Al(NO_3)_3 \cdot 9H_2O$ (0.05 mol) or 17.4 g $Cr(NO_3)_3 \cdot 9H_2O$ or 20.2 g $Fe(NO_3)_3 \cdot 9H_2O$

(initial Zn/Al or Zn/Cr or Zn/Fe =3) with vigorous stirring at 25 ^{o}C until the final pH = 8.5. Then, the resulting slurry was aged at 75 °C for 12 h, and then centrifuged and washed with deionized water until the pH decreased to 7, finally it was dried in vacuo at 65 °C for 12 h, grounded, giving the product ZnAl–LDHs, ZnCr–LDHs and ZnFe–LDHs.

2.3. Synthesis of ZnCe–LDHs.

Under N_2 atmosphere, an aqueous solution (100 mL) containing urea (37.8 g, 0.63 mol) was added dropwise to a solution (120 mL) containing 26.7 g (0.09 mol) of $Zn(NO_3)_2 \cdot 6H_2O$ and 13.1 g $Ce(NO_3)_3 \cdot 6H_2O$ (0.03 mol) with vigorous stirring at 50 ^{o}C until the final pH=8.5. Then, the produced suspension was stirred for 24 h at a refluxing temperature of 105 °C under N_2 atmosphere. The product was centrifuged and washed twice with deionized water and then once with anhydrous ethanol until the pH=7. Finally the sample was dried in vacuo at 65 ^{o}C for 18 h, then ground, giving the product ZnCe–LDHs.

2.4. Preparation of Ti/Schiff–base.

In 250 ml flask, 100ml of ethanol solution containing 6.12 g (50 mmol) salicylaldehyde was added dropwise into a solution containing 6.86 g (50 mmol) of sodium 4–Aminobenzoate and fifty milliliter of ethanol with vigorous stirring for 30 min. Then, the reaction system was continuously stirred for 3 h at a refluxing temperature of 85 °C. The resultant slurry was then condensed, refrigerated, filtered, washed with ice–cold ethanol and dissolved with warm ethanol, after repeating the above–mentioned steps three times, finally the product was dried in vacuo oven at

60 °C for 6 h, giving the Schiff–base ligand ($C_{14}H_{10}NO_3Na$, 263 g/mol, abbreviated as SB, the yield = 62.5%, the content of C, H and N: C = 62.43%, H = 3.57%, N = 5.49%).

An ethanolic solution (60 mL) containing as–synthesized Schiff base ligand (0.711 g, 2.7 mmol) was added dropwise to a solution containing 0.17 ml (1.5 mmol) of $TiCl_4$ and 10ml of ethanol with vigorous stirring under the N_2 atmosphere. Then, the produced suspension was continued stirred for 2 h at a refluxing temperature of 80 °C. The slurry was filtered, washed thrice with ethanol and recrystalized from diethyl ether, finally it was dried in vacuo oven at 65 °C for 6 h, giving the product Ti/Schiff–base complex $(C_{14}H_{10}NO_3Na)_2Ti$, 573.9 g/mol, abbreviated as Ti/SB, the yield = 78.3.%, the content of C, H, N and Ti: C = 58.17%, H = 3.46%, N = 4.85%, Ti = 8.85%).

2.5. Synthesis of Ti/ZnO–M_xO_y composite (M=Al, Cr, Fe, Ce).

First of all, the ion–exchange method was used to synthesize ZnM–Ti/Schiff base–LDHs, and the detailed process was given below: firstly, 100 ml of ethanol was added to 1.0 g dried Zn/M–LDHs (about 5 mmol of M) and stirred for 1 h; secondly, designated quality 2.85 g (5 mmol) of Ti/Schiff–base complex (the molar ratio of Ti/M=1) was transferred into the above mentioned ethanolic suspension of LDHs, and the reaction system was refluxed at 85 ^oC for 24 h with constant stirring; finally, the product was isolated by filtration, washed with ethanol and kept overnight in vacuum at 65 ^oC, giving the product ZnM–Ti/Schiff base–LDHs, abbreviated as ZnM–Ti/SB–LDHs (M=Al, Cr, Fe, Ce).

And then powders, as 1.5 g samples, were calcined in a muffle furnace with feedback–controlled microwave heating in flowing dry air at temperature of 800 ˚C for 4 h, then grounded, giving the product Ti/ZnO–M_xO_y composites (M=Al, Cr, Fe, Ce). The complete preparation pathway for the Ti/ZnO–M_xO_y composites is given in Scheme 1.

2.6. Materials Characterization.

Zn, Al, Cr, Fe, Ce and Ti element analysis was conducted using inductively coupled plasma atomic emission spectrometry (ICP–AES) on a IRIS Intrepid II XSP instrument. C, H, N elemental microanalyses were obtained on a ThermoFinnigan Italia S.P.A elemental analyzer. Powder X–ray diffraction (XRD) patterns were recorded on a Rigaku RINT 2000 powder diffractometer, using Cu Kα radiation (λ = 1.54 Å) at 40 kV and 178 mA and scanning rate of 5°/min in the range of 5–70 °. SEM–EDS analysis was carried out in a Hitachi SU1510 ESEM with an acceleration voltage of 15 kV. The pore structure of the Zn–based LDH materials was analyzed by N_2 adsorption–desorption at 77 K on a Micromeritics Instrument Corporation ASAP2020M apparatus. Prior to the analysis, the samples were degassed in a vacuum at 120 ^{o}C for 6 h. The specific surface areas were calculated by the Brunauer–Emmett–Teller (BET) method, and the pore size distribution and total pore volume were determined by the Brunauer–Joyner–Hallenda (BJH) method. Solid–state UV–vis diffuse reflectance spectra was recorded at room temperature in air by means of a Shimadzu UV–2550 spectrometer equipped with an integrating sphere attachment using $BaSO_4$ as background.

2.7. Photocatalytic Reaction.

The photocatalytic activity of samples was monitored by degradation of Hexachlorobenzene (HCB) under irradiation with visible light using a 300 W xenon lamp (400 nm<λ<800 nm) equipped with a constant temperature circulator at 15 ^{o}C. Typically, in 150 ml reacton, a mixture of 100 mL of HCB (2 mg/L) solution and 100 mg of catalyst (both for LDHs and Ti/ZnO–M_xO_y composite) was vigorously stirred for 30 min to establish an adsorption/desorption equilibrium in dark. Then the reaction solution was stirred under visible light irradiation for 210 min (LDHs) and 240 min (Ti/ZnO–M_xO_y composite) under the constant temperature at 25 ^{o}C. At given time intervals (for example, 5 min interval, 10 min interval, 20 min interval and 30 min interval), 2 mL aliquots were sampled and filtered to remove the solid phase. The concentration of HCB in filtrate was tested by HPLC or GC and the blank reaction was also carried out by the same procedure without adding any catalyst.

3. Results and Discussion

3.1. Structural characteristics of samples

On the basis of ICP–AES and CHN analytic results, the chemical composition of LDHs and Ti/ZnO–M_xO_y composites was determined and the results were listed in Table 1. As shown in Table 1, the simplest molecular formula of these Zn–based LDHs was as follow: $Zn_{0.74}Al_{0.26}(OH)_2(NO_3^-)_{0.32}$ $0.39H_2O$, $Zn_{0.74}Cr_{0.26}(OH)_2(NO_3^-)_{0.32}$ $0.41H_2O$, $Zn_{0.73}Fe_{0.27}(OH)_2(NO_3^-)_{0.33}$ $0.43H_2O$ and $Zn_{0.77}Ce_{0.23}(OH)_2(NO_3^-)_{0.31}$ $0.40H_2O$. It is clear that the experimental results are in good agreement with the prospective products.

Figure 1(A and B) showed the XRD patterns of ZnM–LDHs and ZnM–Ti/SB–LDHs. The expected peaks of 003, 006, 009, 110 and 113 were observed in all the sample of ZnM–LDHs, which indicated the successful synthesis of typical LDH material. And the interlayer distance (d_{003}) of ZnAl–LDHs, ZnCr–LDHs, ZnFe–LDHs and ZnCe–LDHs was 0.874 nm (2θ=11.2 ^{o}), 0.889 nm (2θ=10.5 ^{o}), 0.777 nm (2θ=11.3 ^{o}) and 0.892 nm (2θ=10.4 ^{o}), respectively. It was consisted with the results reported by other authors [25–28]. Moreover, after intercalation, for ZnM–Ti/SB–LDHs, the typical peaks of LDHs were also appeared, and the interlayer distance (d_{003}) increased to 1.285 nm (2θ=6.9 ^{o}) for ZnAl–Ti/SB–LDHs, 1.290 nm (2θ=6.8 ^{o}) for ZnFe–Ti/SB–LDHs, 1.729 nm (2θ=4.8 ^{o}) both for ZnCr–Ti/SB–LDHs and ZnCe–Ti/SB–LDHs, respectively. It indicated that the gallery height of these samples after ion–exchange was all increased which can be calculated by the interlayer distance minus the thickness of the LDH layers (0.48 nm) [29]. The increment of gallery height confirmed the successful intercalation of the Ti/SB complex and formation of organic–inorganic hybrid materials.

Figure 1(C) was the XRD patterns for Ti/ZnO–M_xO_y composites. As expected, after calcination, the XRD curves for composites not only showed the completely destruction of layered structure of the original LDHs, but also indicated the appearance of new peaks of metal oxides contained ZnO, Al_2O_3, Cr_2O_3, Fe_2O_3, CeO_2, TiO_2, and spinel phase, such as $ZnAl_2O_4$, $ZnCr_2O_4$, $ZnFe_2O_4$, $ZnTiO_3$ and so on [30–32]. Particularly, compared with ZnM–LDHs and ZnM–Ti/SB–LDHs (M=Cr and Ce), the basic lines for Ti/ZnO–Cr_2O_3 and Ti/ZnO–CeO_2 composites were much lower and even, the peaks were much sharper and intense, which indicated the highly crystalline structures of the latters.

The SEM images of LDHs (ZnCr–LDHs was chose as a sample) and Ti/ZnO–M_xO_y composites were given in Fig. 2. The ZnCr–LDHs sample (Fig. 2A and B) displayed layered platelet–shape morphology with sharp edges which confirm the formation of well–ordered LDH materials. Fig. 2C was the SEM image for Ti/ZnO–Cr_2O_3 composite, which indicated the formation of somewhat regular–shaped aggregates. Particularly, the SEM picture of Ti/ZnO–Cr_2O_3 composite with high–magnification (Fig 2D) showed the appearance of regular flower–shape morphology with agglomerated flake crystals onto the composite particles' surfaces. It showed that after calcination, the original layered morphology LDHs particles convert into composite of metal oxides with regular morphology stacking particles due to the collapse of layers. In addition, the result of EDS analysis (Fig. 2H) showed that main content of the composite was Zn, Cr and Ti elements. Figure 2E, F and G were SEM images of Ti/ZnO–Al_2O_3, Ti/ZnO–Fe_2O_3 and Ti/ZnO–CeO_2, respectively. From which we could see that all of three samples had the similar crystal form structure with Ti/ZnO–Cr_2O_3 composite. Thus, it could be concluded that Ti/ZnO–M_xO_y composite with highly dispersed of Ti elements could be obtained from calcination of Ti/Schiff base intercalated ZnM–LDHs at high temperature.

For further investigation of the textural parameters of samples, nitrogen sorption measurement was carried out. Figure 3 showed the N_2 adsorption–desorption isotherm at 77 K and the corresponding pore size distribution curves for ZnM–LDHs and Ti/ZnO–M_xO_y composite. The isotherms for ZnM–LDHs (Figure 3A–D) were all type II with broad H3 type hysteresis loop ($P/P_0<0.4$), indicating the presence of

mesopores. And any limiting adsorption at higher P/P_0 was not observed, indicating the existence of macropores [33]. This result could be confirmed by the corresponding wide distribution of pore size in Fig. 3A–D insert. And the surface area for ZnM–LDHs followed the order: ZnCr–LDHs (109 m^2/g) > ZnCe–LDHs (101 m^2/g) > ZnFe–LDHs (95 m^2/g) > ZnAl–LDHs (88 m^2/g).

In addition, all of the isotherms for Ti/ZnO–M_xO_y composites were type IV (Fig. 3E–H), which were assigned to mesoporous structure, according to the IUPAC classification [34]. Hysteresis loops were of type H3, which were commonly attributed to slit–shaped pores generated by the aggregation of particles. Particularly, although isotherms for composites were somewhat similar, there were obvious differences in surface area, pore volume and pore size distribution. First of all, Ti/ZnO–M_xO_y composites showed larger surface area, smaller pore volume and narrower pore size distribution than that of ZnM–LDHs. Secondly, the surface area for Ti/ZnO–M_xO_y composites also followed the order: Ti/ZnO–Cr_2O_3 (227 m^2/g) > Ti/ZnO–CeO_2 (199 m^2/g) > Ti/ZnO–Fe_2O_3 (178 m^2/g) > Ti/ZnO–Al_2O_3 (155 m^2/g), which was in good agreement with ZnM–LDHs. In addition, Ti/ZnO–Cr_2O_3 composite showed smaller pore volume and narrower pore size distribution among four metal oxides composites (see Table 2). So, it was obvious that the physico–chemical property of materials was greatly improved after caicination of Ti/Schiff base intercalated LDHs at high temperature, especially for Ti/ZnO–Cr_2O_3 composite.

The UV−vis results shown in Fig. 4 were used to calculate the band gaps of ZnM–LDHs and Ti/ZnO–M_xO_y composite. And the plots of $(\alpha h\upsilon)^2$ *vs* $h\upsilon$ for the materials based on Eq. (1) was also given in Fig. 4.

$$\alpha h\upsilon = K(h\upsilon - E_g)^{n/2} \quad (1)$$

where α, h, υ, K, and E_g are the absorption coefficient, planck constant, light frequency, proportionality constant, and band gap, respectively. In addition, n decides the characteristics of the transition in a semiconductor: n = 1 is for a directly allowed transition and n = 4 is for indirectly allowed transition. The values of n and E_g can be determined by the following steps: firstly, plot ln ($\alpha h\upsilon$) vs. ln ($h\upsilon - E_g$), using an approximate value of E_g, and then determine the value of n with the slope of the straightest line near the band edge. When this method was used, the n value was 1, indicating the directly allowed optical transition. Secondly, plot $(\alpha h\upsilon)^{2/n}$ vs. $h\upsilon$ and then the band gap E_g can be obtained by extrapolating the linear region straight line to the $h\upsilon$ axis intercept. The optical band gap energies of the samples were also shown in Table 2. It could be seen that the band gap of ZnM–LDHs was from 2.77 to 3.23 eV, while, after intercalation and calcination, the values for Ti/ZnO–M_xO_y composites were reduced to 2.40–2.80 eV. And all of the composites had narrower band gap than that of original LDHs. In addition, the band gap of Ti/ZnO–M_xO_y composites also followed the order: Ti/ZnO–Cr_2O_3 (2.40 eV) > Ti/ZnO–CeO_2 (2.68 eV)>Ti/ZnO–Fe_2O_3 (2.75 eV) > Ti/ZnO–Al_2O_3 (2.80 eV), respectively.

To better understand the electronic band structure of ZnM–LDHs and Ti/ZnO–M_xO_y composites, periodic density functional theory (DFT) calculation was performed to illustrate the total and partial electronic density of states (TDOS and

PDOS) and the results are shown in Fig. 5. It is known that the conventional DFT method always underestimates the band band gap of semiconductors [35]. For the purpose of researching the objective composition of ZnM–LDHs and Ti/ZnO–M_xO_y composite best, we made some optimization for the calculation parameter and models, which was given in supporting materials. Firstly, the periodical model of $Zn_6M_2(OH)_{16}(NO_3^-)_2$ was established in hexagonal (2H) stacking sequence, containing $Zn_3M(OH)_8^+$ as host layer and NO_3^- as guest anion. In addition, the designated mole ratios of M_xO_y and TiO_2 were used to replace the adjacent ZnO (see Figure S1). The calculations were carried out by the software Materials Studio 5.5 with the CASTEP code. The composition of electronic band structure could be analyzed by the density of states (DOS), and the bottoms of conduction band and the tops of valance band could be clarified [36,37]. It could be seen from Figure 5 that the calculated band gaps of the materials are 2.91 eV, 2.54 eV, 2.79 eV and 2.63 eV for ZnM–LDHs; 2.48 eV, 2.25 eV, 2.41 eV and 2.33 eV for Ti/ZnO–M_xO_y composites, respectively, which was also given in Table 2. These calculation results were in good agreement with UV–vis analysis.

In addition, the electronic density of states of all elements for Ti/ZnO–M_xO_y composite was shown in Fig. S2. For Ti/ZnO–Al_2O_3 and Ti/ZnO–Fe_2O_3, the top of the VB and the bottom of the CB are mainly dominated by the 2s, 2p orbitals of O, 3p, 4s of Zn, 3s, 3 p of Al or Fe, and 3d of Ti, from the metal oxides contribute to the TDOS; and for Ti/ZnO–Cr_2O_3 and Ti/ZnO–CeO_2, 2p of O, 4s, 3p of Zn, 3p and 3d orbitals of Cr, Ce and Ti contributed a lot to the TDOS. The narrower band gap of Ti/ZnO–M_xO_y composite is may result from the influence of M and Ti elements by intercalation and calcinations of the LDH sample, especially for Cr and Ce.

3.2. Photocatalytic properties of Ti/ZnO–M_xO_y composite

The investigation for HCB photodegradation by Ti/ZnO–M_xO_y composites was carried out at the condition of 0 to 240 min, 25 ^oC, pH=7.0, [HCB]=2.0 mg/L and using 100 mg of catalyst under visible light. The photodegradation curves were presented in Fig. 6. The result of blank experiment showed that HCB was very stable, and the self–decomposition amount was only 3% after 240 min in dark. Moreover, it could be seen that the photodegradation curves for HCB by ZnM–LDHs were relatively gentle, the decomposition amount of HCB were almost no changed after 180 min, and the values were only 25.5%–33.6%. Nevertheless, when Ti/ZnO–Cr_2O_3 composites were used as photocatalysts, all of the degradation curves showed that the concentration of HCB decreased rapidly in the initial 60 min and almost unchanged after 240 min, indicating reaching an equilibrium state, the values for Ti/ZnO–Al_2O_3, Ti/ZnO–Cr_2O_3, Ti/ZnO–Fe_2O_3 and Ti/ZnO–CeO_2 were 75.2%, 95.1%, 80.6% and 89.4%, respectively. It was obviously that the decomposition amount of HCB was greatly increased than that of ZnCr–LDHs. The activity for HCB degradation by Ti/ZnO–Cr_2O_3 was 4.75 mg/g·h, which was much more efficient and effective than other reported photocatalysts [38–40]. Furthermore, Figure 6B was the photodegradation curves of total organic carbon (TOC) concentration by ZnCr–LDHs and Ti/ZnO–Cr_2O_3 composite under visible–light irradiation. It could be seen that the TOC removal rate was quite consistent with the HCB photodegradation, it proved that HCB could be decomposed under the catalyst and visible light, the benzene ring was opened up, also the decrease of total carbon could be caused by the formation of small molecules such as CO_2 and H_2O.

As a sample, Ti/ZnO–Cr_2O_3 was chosen to discuss the reutilization of those metal oxide composites as efficient photocatalysts to decompose HCB. The thermal regeneration experiments were carried out and the results were shown in Fig. S3. It showed that the progressive reduction after fifth–cycles regeneration was very small, the decomposition of HCB was 95.1%, 93.9%, 92.6%, 91.5%, 90.3%and 89.0% for original composite, first–, second–, third–, fourth– and fifth–cycle, respectively. It indicated that Ti/ZnO–Cr_2O_3 composite was stable enough as photocatalyst for HCB degradation, and the thermal regeneration for re–use of this material was feasible for at least five cycles.

3.3. The discussion about relationship between supramolecular structure, physico–chemical property of catalysts and their photocatalytic performacne

Particularly, according to XRD analysis, the interlayer distance (d_{003}) increased to 1.285 nm for ZnAl–Ti/SB–LDHs, 1.729 nm for ZnCr–Ti/SB–LDHs, 1.290 nm for ZnFe–Ti/SB–LDHs and 1.729 nm for ZnCe–Ti/SB–LDHs. And the thickness of the LDH layer was 0.48 nm, the gallery height of LDH after intercalation was 0.805 nm, 1.249 nm, 0.810 nm and 1.249 nm, respectively, which could be calculated by the interlayer distance minus the thickness of the LDH layer. The long axis, short axis and molecular thickness of Ti/SB complex were 1.2386 nm, 0.8037 nm and 0.8037 nm, respectively, which could be calculated from the PM3 semi–empirical molecular orbital method of Gaussian 09 software.

The gallery height of ZnAl–Ti/SB–LDHs and ZnFe–Ti/SB–LDHs was 0.805 and 0.810 nm, which was similar with the value of short axis or thickness of Ti/SB

complex (0.8037). It suggested that the Ti/SB ligand anions were alternately intercalated along the orientation of short axis or thickness for Ti/SB complex between layers with the carboxyl of adjacent anion attaching to the upper or lower hydroxide layers. The schematic representation of the probable arrangement for ZnAl–Ti/SB–LDHs and ZnFe–Ti/SB–LDHs was shown in Fig. 7A. While in the case of ZnCr–Ti/SB–LDHs and ZnCe–Ti/SB–LDHs, the value of long axis (1.2386 nm) was well consisted with the gallery height of intercalated LDHs (1.249 nm). It indicated that the orientation of guests in LDH interlayer were accommodated as alternately and monolayer vertical (along the long axis for Ti/SB). And the negative group of adjacent anions attracted electrostatically to both upper and lower hydroxide layers, as depicted in Fig. 7B.

Generally speaking, the supramolecular structure materials contained guests with negative group of adjacent anions attracted to both upper and lower hydroxide layers has larger supramolecular acting force, hydrogen bond and electrostatic interaction than that of the anions attracted to either upper or lower layers [41]. Thus, the stability for former was higher than the latter.

Based on the energy band theory, when metal oxides absorbed photons with energy higher than its band gap, the excited electrons of material were promoted from the valence band to the conduction band yielding holes (h^+) and photon generated electrons (e^-). The electrons and holes reacted with the O_2 and H_2O absorbed at the surface of metal oxides to produce highly active radicals such as hydroxide radicals (·OH), superoxide radicals ($\cdot O_2^-$) and peroxide free radicals (·OOH). Essentially the

photocatalytic degradation of organic compounds was a radial reaction. The intermediate radicals could oxidize all different organic compouds directly into small inorganic compounds such as CO_2 and H_2O. Thus, to determine the radicals and explain the catalytic reaction mechanism of Ti/ZnO–M_xO_y composites during the photocatalytic degradation of HCB, we used ESR technique to characterize the reaction with ZnCr–LDHs and Ti/ZnO–Cr_2O_3 composite. The results were shown in Fig. 8. As we can see, there was no radical for ZnCr–LDHs under dark condition, while, it showed overlapping peaks for DMPO–$\cdot O_2^-$, DMPO–·OOH and DMPO–·OH after visible light irradiation. Similarly, Ti/ZnO–Cr_2O_3 composite also had no radical signal during ESR test without light exposure, while, it showed typical intense peaks of DMPO–·OH and overlapping small peaks for DMPO–$\cdot O_2^-$ and DMPO–·OOH when material was exposed under visible light. This result indicated that the oxidation reaction was mainly gone through the hydroxyl radicals.

In order to investigating the influence of hydroxyl radicals into the photocatalytic property of HCB by Ti/ZnO–M_xO_y composites, isopropanol (2.0 g/L) was used as a trapping agent for hydroxyl radicals ($CH_3CHOHCH_3 + \cdot OH \rightarrow CH_3C\cdot(OH)CH_3 + H_2O$). The HCB photodegradation contrast between inhibitor and no inhibitor were shown in Fig. 9A. It could be seen that the HCB removal rate decreased from 95.1% to 51.8% when isopropanol was added. It was obviously that the concentration of hydroxyl radicals would greatly influenced the photocatalytic property of composite. Thus, the amount of hydroxyl radicals produced by four composite photocatalytic systems was further determined

using salicylaldehyde spectrophotometry [42], which was shown in Figure 9B. The result showed that the photocatalyst obtained from supramolecular system with larger interlayer distance (Ti/ZnO–CeO_2 and Ti/ZnO–Cr_2O_3) may produce more hydroxyl radicals than that of system with small interlayer distance (Ti/ZnO–Al_2O_3 and Ti/ZnO–Fe_2O_3).

Many studies had been proved that it would be an energy band coupling effect on the phase interface during the combination of different semiconductor materials [43–45]. In this condition, electron–hole pairs produced from surface of the semiconductors would migrate along the vector orientation. This migration was very benefit for the photocatalytic property of the materials due to the effective inhibition of the quick recombination of electron–hole pairs. ZnO–based semiconductor composites which had been reported contain ZnO/SnO_2, ZnO/NiO, ZnO/TiO_2, and so on [43–45]. Thus, it would be an energy band coupling effect on the phase interfaces of Ti/ZnO–M_xO_y composite. For example, Ti/ZnO–Cr_2O_3, under the visible light irradiation, electron–hole pairs produced from surface of the metal oxides (ZnO/Cr_2O_3/TiO_2) would migrate along the vector orientation. The migration would effectively inhibit the quick recombination of electron–hole pairs (Scheme 2).

Furthermore, there would be two reasons that Ti/ZnO–Cr_2O_3 and Ti/ZnO–CeO_2 showed higher photocatalytic performances than Ti/ZnO–Fe_2O_3 and Ti/ZnO–Al_2O_3. One reason was that Ti/ZnO–Cr_2O_3 and Ti/ZnO–CeO_2 showed narrower band gap, larger surface area and much more uniform pore size distribution than that of the latter two. The other was that, for layered supramolecular structure material, the more strength supramolecular and electrostatic interaction it had, the more hydroxyl radicals would be produced after calcination of layered material. Thus, the corresponding composite (Ti/ZnO–Cr_2O_3 and Ti/ZnO–CeO_2) would show higher

photocatalytic performance for HCB degradation than Ti/ZnO–Fe_2O_3 and Ti/ZnO–Al_2O_3. The schematic diagram for relationship between supramolecular structure and photocatalytic performance of different Ti/ZnO–M_xO_y composites was shown in Scheme 3.

3.4. Photocatalytic intermediates and pathway for HCB degradation by Ti/ZnO–M_xO_y composite

The degradability of chlorobenzene compounds decreased as the chloro–number increased. Chlorine element could strongly attract the electronic cloud and decrease the electron density on the benzene ring, which made electrophilic reaction more difficult [46]. This could be the reason that detailed photocatalytic reaction mechanism reported for hexachlorobenzene (HCB) degradation was very little. In this paper, we used GC–MS and HPLC–MS to study the reaction intermediates during the photocatalytic degradation of HCB at the Ti/ZnO–M_xO_y composite surface. And the detailed information was given in supporting materials (Figure S4–S7).

From GC–MS spectrum during the degradation reaction, we could categorize the intermediates into three major groups:

The first group was the chlorobenzene compounds with low chloro–number, which included pentachlorobenzene, tetrachlorobenzene. The OH radicals caused the HCB degradation by attacking the C–Cl bond, Cl was removed to produce such chlorobenzene compounds.

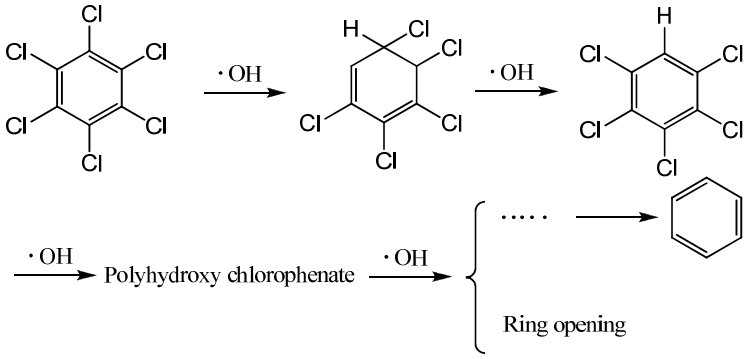

The second kind of intermediate was mainly the chlorophenols such as pentachlorophenol, dichlorophenol, etc. Because OH group was the electron contributing group, it enriched the electron density and increased the benzene ring activity. The ·OH radical would react with HCB molecule by substitution reaction. Therefore when attacked again by ·OH, HCB tended to form chlorophenol with low chloro–number.

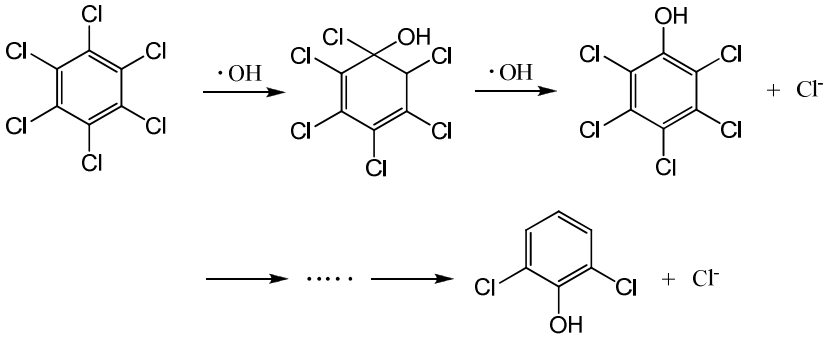

The third group of compounds was originated from the ring opening reaction. Based on HPLC–MS analysis, these compounds were formic acid, acetic acid, oxalic acid. When HCB was attacked by ·OH through substitution/elimination reaction to form products such as pentachlorobenzene, tetrachlorobenzen, pentachlorophenol and bichlorophenol, the OH group enriched the electron density of the ring and activate it, therefore the other Cl atoms were becoming easier to be substituted by ·OH and generate polyhydroxy benzene. Polyhydroxy benzene was unstable and tended to go

through ring opening reaction to generate smaller acids which was further mineralized as H_2O and CO_2.

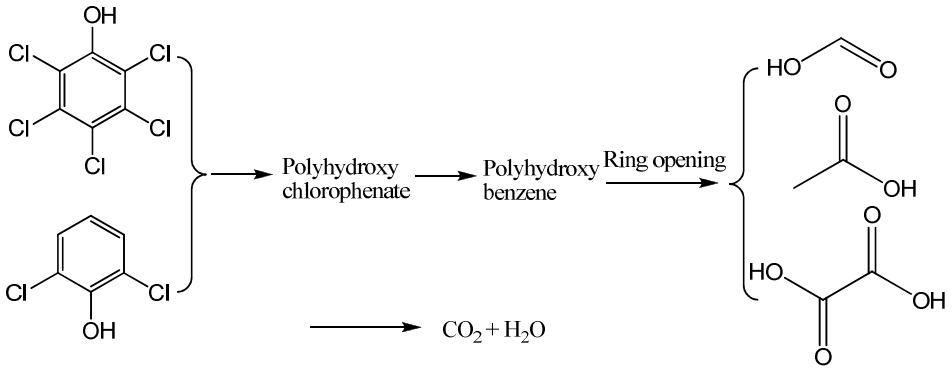

Based on the analysis mentioned above, we considered the HCB photocatalytic degradation included the following steps: phenoxy–reaction of HCB, C–Cl bond break, hydroxylation of benzene ring, benzene ring opening. The schematic diagram of whole photodegradation process for HCB was shown in Scheme 4.

Acknowledgment

This work is supported by Natural Science Foundation of China (21503188) and Zhejiang Provincial Natural Science Foundation of China (LQ15B030002).

4. Conclusions

A series of ZnM–LDHs were intercalated by Ti/Schiff base complex to form novel Ti–contained layered organic–inorganic hybrid materials. And these hybrid materials were further calcined to prepare the metal oxide composites (Ti/ZnO–M_xO_y, M=Al, Cr, Fe, Ce). Based on the characterization results from ICP–AES, XRD, SEM and BET analyses, it could be concluded that the obtained Ti/ZnO–M_xO_y composite with highly dispersed Ti elements showed good crystalline structure, large surface area and

uniform pore size distribution. Moreover, the electronic band structure of LDHs and composites were analyzed by periodic density functional theory (DFT) calculation, which was in good agreement with the experimental result from UV–vis (the value of band gap: Ti/ZnO–Cr_2O_3<Ti/ZnO–CeO_2<Ti/ZnO–Fe_2O_3<Ti/ZnO–Al_2O_3). In addition, Ti/ZnO–M_xO_y composites showed much higher photocatalytic activity than original ZnM–LDHs for HCB degradation, due to the advantages of narrower band gap, special flower–like crystal morphology, larger surface area and more uniform pore size distribution. The highest efficiency for HCB photodegradation was 95.5% after 240 min of reaction when Ti/ZnO–Cr_2O_3 was used as catalyst (4.75 mg/g·h). The experimental and theoretical results also showed that, for layered supramolecular structure material, the more strength supramolecular and electrostatic interaction it had (larger interlayer distance), lower band gap and the more hydroxyl radicals would be produced after calcination of layered material. Thus, the corresponding composite (Ti/ZnO–Cr_2O_3 and Ti/ZnO–CeO_2) would show higher photocatalytic performance for HCB degradation than Ti/ZnO–Fe_2O_3 and Ti/ZnO–Al_2O_3. The oxidation reaction was mainly gone through hydroxide radicals and the decomposition intermediates for HCB were pentachlorobenzene, tetrachlorobenzene, pentachlorophenol, dichlorophenol and benzene.

References

[1] G.L. Fan, F. Li, D.G. Evans, X. Duan, Chem. Soc. Rev. *Chem. Soc. Rev.* **2014**, 43, 7040–7066.

[2] M.J. Climent, A. Corma, S. Iborra, Chem. Rev. *Chem. Rev.* **2011**, 111, 1072–1133.

[3] G.R. Patzke, Y. Zhou, R. Kontic, F. Conrad, *Angew. Chem. Int. Edit.* **2011**, 50, 826–859.

[4] M.Q. Zhao, Q. Zhang, J.Q. Huang, F. Wei, *Adv. Funct. Mater.* **2012**, 22, 675–694.

[5] T. Nakato, H. Ueda, S. Hashimoto, R. Terao, M. Kameyama, E. Mouri, *ACS Appl. Mater. Inter.* **2012**, 4, 4338–4347.

[6] J.S. Valente, F. Tzompantzi, J. Prince, *Appl. Catal. B* **2011**, 102, 276–285.

[7] Z.J. Huang, P.X. Wu, Y.H. Lu, X.R. Wang, N.W. Zhu, Z. Dang, *J. Hazard. Mater.* **2013**, 246–247, 70–78.

[8] D. Carriazo, M. del Arco, E. Garcia–Lopez, G.nMarci, C. Martin, L. Palmisano, V. Rives, *J. Mol. Catal. A–Chem.* **2011**, 342–43, 83–90.

[9] Y. Lee, J.H. Choi, H.J. Jeon, K.M. Choi, J.W. Lee, J.K. Kang, *Energ. Environ. Sci.* **2011**, 4, 914–920.

[10] J. Prince, F. Tzompantzi, G. Mendoza–Damian, F. Hernandez–Beltran, J.S. Valente, *Appl. Catal. B* **2015**, 163, 352–360.

[11] X.R. Wang, , P.X. Wu, , Z.J. Huang, , N.W. Zhu, J.H. Wu, P. Li, Z. Dang, *Appl. Clay Sci.* **2014**, 95, 95–103.

[12] Y.F. Zhao, P.Y. Chen, B.S. Zhang, D.S. Su, S.T. Zhang, L. Tian, J. Lu, Z.X. Li, X.Z. Cao, B.Y. Wang, M. Wei, D.G. Evans, X. Duan, *Chem–Eur. J.* **2012**, 18, 11949–11958.

[13] C. Alanis, R. Natividad, C. Barrera–Diaz, V. Martinez–Miranda, J. Prince, J.S. Valente, *Appl. Catal. B* **2013**, 140, 546–551.

[14] L. Mohapatra, K.M. Parida, *Phys. Chem. Chem. Phys.* **2014**,16, 16985–16996.

[15] H.Y. Jing, T. Wen, C.M. Fan, G.Q. Gao, S.L. Zhong, A.W. Xu, *J. Mater. Chem. A* **2014**, 2, 14563–14570.

[16] X.R. Wang, P.X. Wu, Y.H. Lu, Z.J. Huang, N. W. Zhu, C. Lin, Z. Dang, Sep. Purif. Technol. 132 (2014) 195–205.

[17] Z. Bouberka, K. A. Benabbou, A. Khenifi, U. Maschke, *J. Photoch. Photobio. A* **2014**, 275, 21–29.

[18] V. Elango, H.D. Kurtz, D.L. Freedman, *Chemosphere* **2011**, 84, 247–253.

[19] B. Camacho–Perez, E. Rios–Leal, N. Rinderknecht–Seijas, H.M. Poggi–Varaldo, *J. Environ. Manage.* **2012**, 95, S306–S318.

[20] J.W. Li, P. Zhao, S.T. Liu, *Appl. Catal. A–Gen.* **2014**, 482, 363–369.

[21] S. Maddila, V.D.B.C. Dasireddy, E.O. Oseghe, S.B. Jonnalagadda, *Appl. Catal. B* **2013**, 142, 129–141.

[22] J.A. Cecilia, I. Jiménez–Morales, A. Infantes–Molina, E. Rodríguez–Castellón, A. Jiménez–López, *J. Mol. Catal. A–Chem.* **2013**, 368–369, 78–87.

[23] B.B. Yu, J.B. Zeng, L.F. Gong, M.S. Zhang, L.M. Zhang, X. Chen, *Talanta* **2007**, 72, 1667–1674.

[24] S.J. Xia, F.X. Liu, Z.M. Ni, W. Shi, J.L. Xue, P.P. Qian, *Appl. Catal. B* **2014**, 144, 570–579.

[25] P. Koilraj, R.S. Thakur, K. Srinivasan, *J. Phys. Chem. C* **2013**, 117, 6578–6586.

[26] K.M. Parida, L. Mohapatra, *Chem. Eng. J.* **2012**, 179, 131–139.

[27] C.G. Silva, Y. Bouizi, V. Fornes, H. Garcia, *J. Am. Chem. Soc.* **2009**, 131, 13833–13839.

[28] Z.P. Liu, R.Z. Ma, Y. Ebina, N. Iyi, K. Takada, T. Sasaki, *Langmuir* **2007**, 23 861–867.

[29] Q. Wang, D. O'Hare, *Chem. Rev.* **2012**, 112, 4124−4155.

[30] S. Cho, J.W. Jang, K.J. Kong, E.S. Kim, K.H. Lee, J.S. Lee, *Adv. Funct. Mater.* **2013**, 23, 2348–2356.

[31] A.Venugopal, R. Sarkari, C. Anjaneyulu, V. Krishna, M.K. Kumar, N. Narender, A.H. Padmasri, *Appl. Catal. A–Gen.* **2014**, 469, 398–409.

[32] S.V. Prasanna, P.V. Kamath, C. Shivakumara, *Mater. Res. Bull.* **2007**, 42, 1028–1039.

[33] J. Yu, S. Liu, H.Yu, *J. Catal.* **2007**, 249, 59–66.

[34] F. Al–Wadaani, E.F. Kozhevnikova, I.V. Kozhevnikov, *J. Catal.* **2008**, 257, 199–205.

[35] J. Tang, Z. Zou, J. Ye, *J. Phys. Chem. C* **2007**, 111, 12779–12785.

[36] H. Yu, H. Irie, K. Hashimoto, *J. Am. Chem. Soc.* **2010**, 132, 6898–6899.

[37] J. Sato, H. Kobayashi, Y. Inoue, *J. Phys. Chem. B* **2003**, 107, 7970–7975.

[38] S. Antonaraki, T.M. Triantis, E. Papaconstantinou, A. Hiskia, *Catal. Today.* **2010**, 151, 119–124.

[39] S.Y. Lu, Q.L. Wang, D. Wu, X.D. Li, J.H. Yan, *Environ. Prog. Sustain.* **2013**, 32, 458–464

[40] F.X. Li, X.H. Lu, X.B. Li, P. Mei, *Fresen. Environ. Bull.* **2009**, 18, 628–632.

[41] J.J. Perry, J.A. Perman, M.J. Zaworotko, *Chem. Soc. Rev.* **2009**, 38, 1400–1417.

[42] H. Li, X.H. Li, D.J. Peng, H.L. Zheng, *Spectrosc. Spect. Anal. (China)* **2007**, 27, 1591–1595.

[43] Z.Y. Wang, B.B. Huang, Y. Dai, X.Y. Qin, X.Y. Zhang, P. Wang, H.X. Liu, J.X. Yu, *J. Phys. Chem. C* **2009**, 113, 4612–4617.

[44] L.R. Zheng, Y.H. Zheng, C.Q. Chen, Y.Y. Zhan, X.Y. Lin, Q. Zheng, K.M. Wei, J.F. Zhu, *Inorg. Chem.* **2009**, 48, 1819–1825.

[45] L.W. Zhang, H.B. Fu, Y.F. Zhu, *Adv. Funct. Mater.* **2008**, 18, 2180–2189.

[46] G.J. Su, H.J. Lu, L.X. Zhang, A.Q. Zhang, L.Y. Huang, S. Liu, L.W. Li, M.H. Zheng, *Environ. Sci. Technol.,* **2014**, 48, 6899–6908.

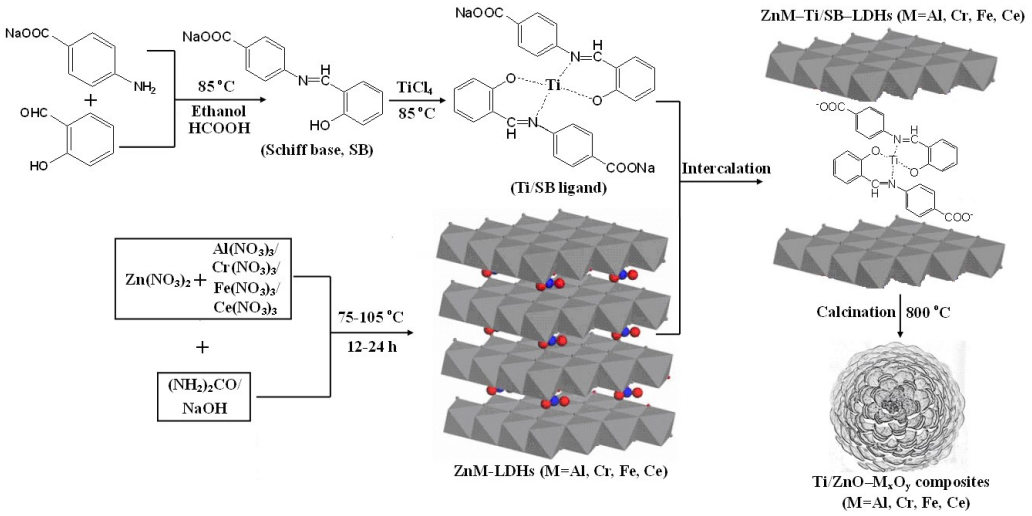

Scheme 1 The preparation pathway for the Ti/ZnO–M_xO_y composites (M=Al, Cr, Fe, Ce).

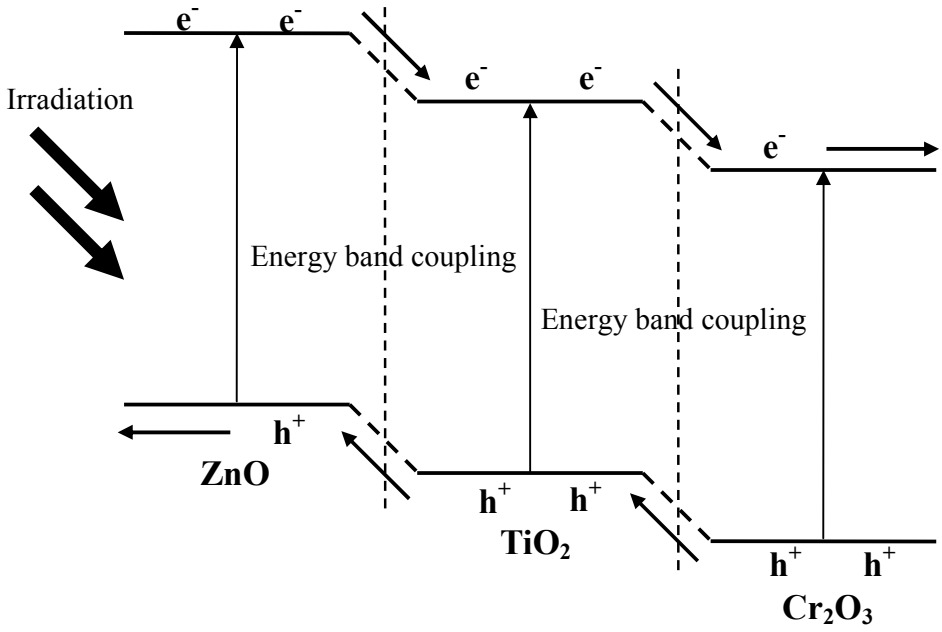

Scheme 2 The schematic diagram of the energy band levels and the transfer procedure of photogenerated e^- and h^+ pairs for Ti/ZnO–Cr_2O_3 composite.

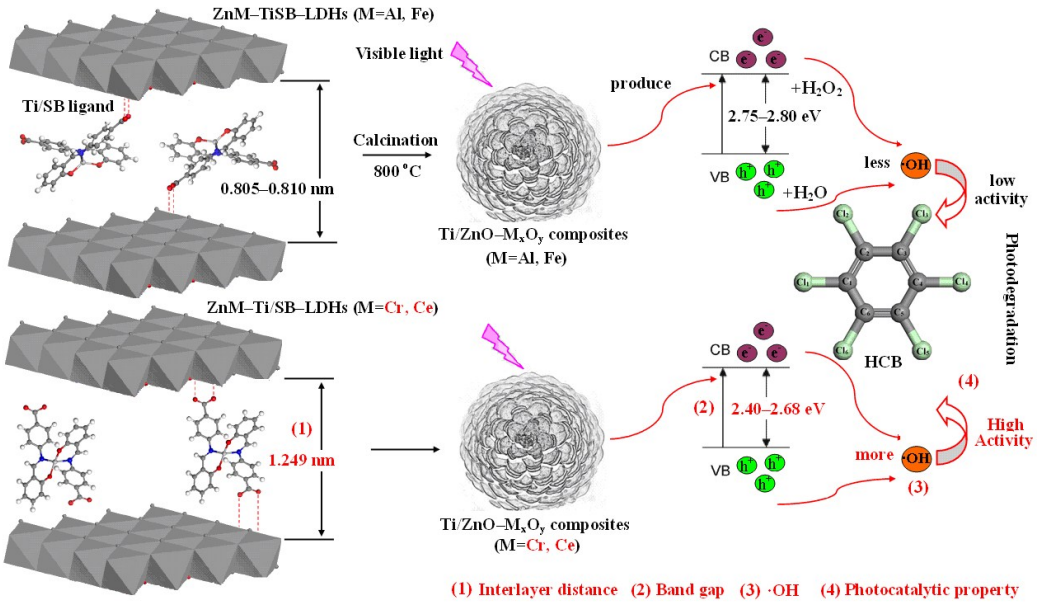

Scheme 3 The schematic diagram for relationship between supramolecular structure and photocatalytic performance of different Ti/ZnO–M_xO_y composites.

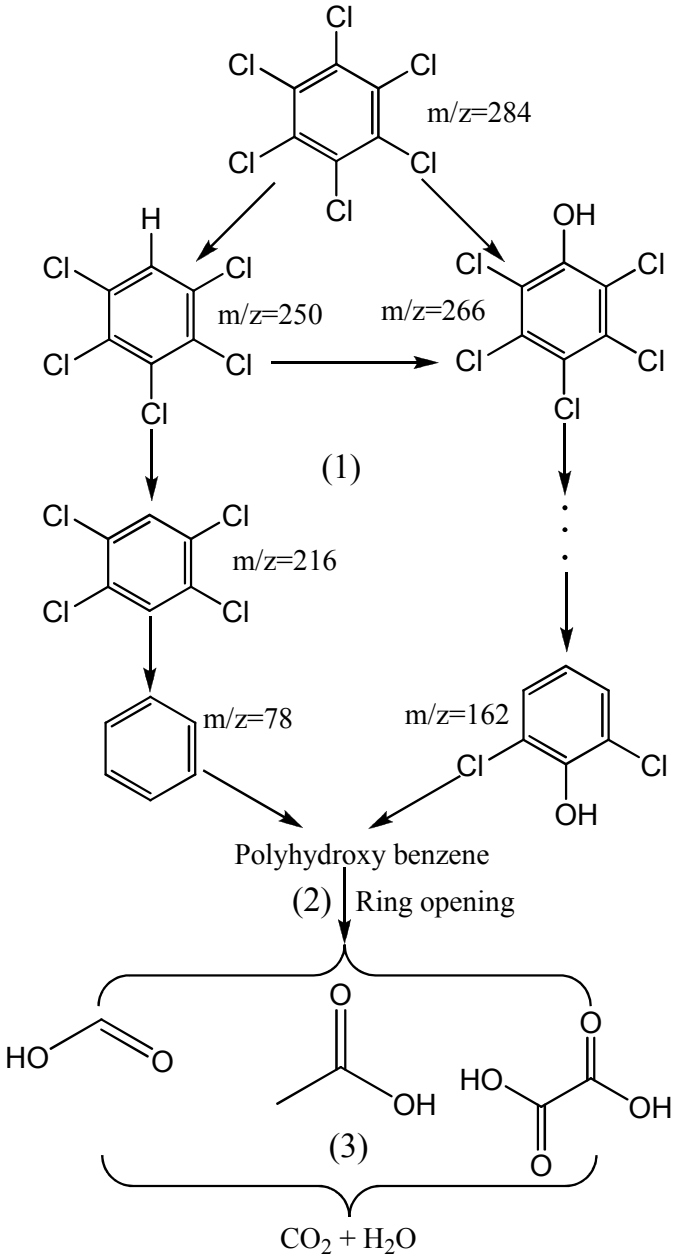

Scheme 4 The whole degradation pathway for HCB.

Note: (1) HCB substitution/elimination reaction, forming low chloro number chlorobenzene and chlorophenols; (2) The generation of smaller organic acid by ring opening reaction of low chloro number chlorobenzene and chlorophenols; (3) The oxidation of organic acids.

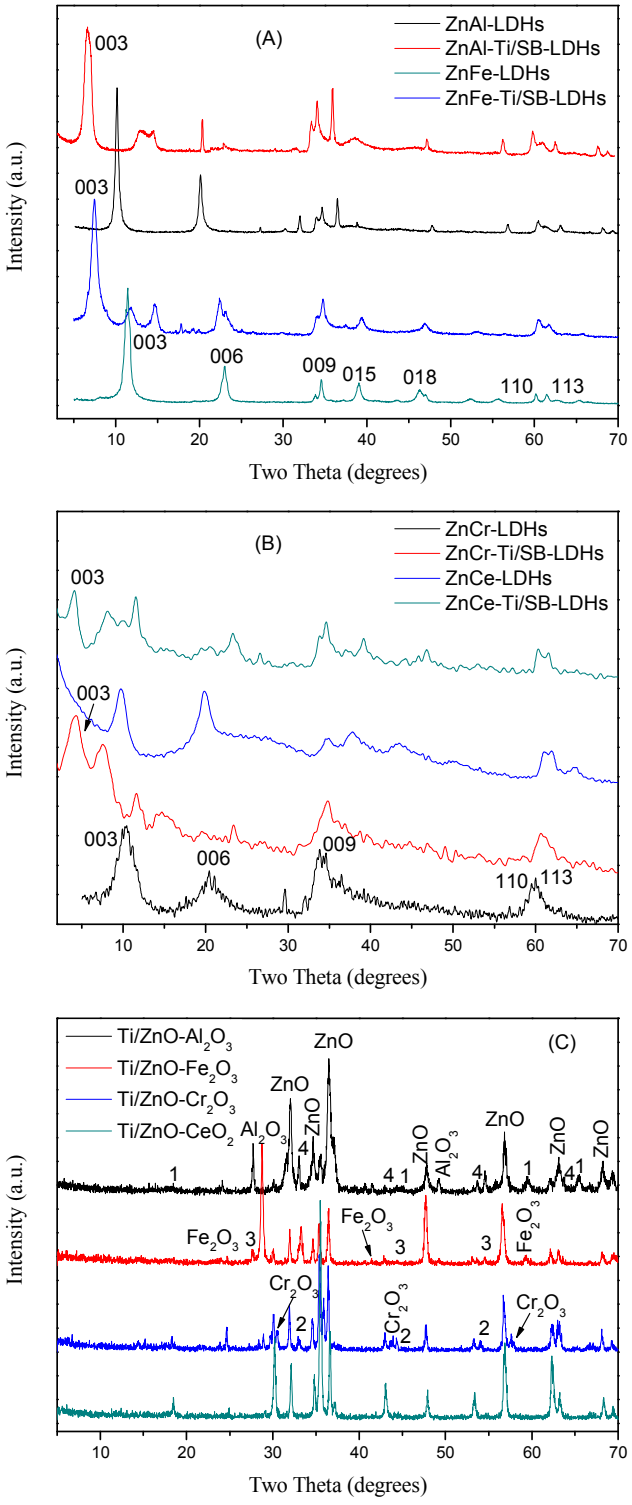

Figure 1 The XRD patterns for ZnM–LDHs (A, B) and Ti/ZnO–M_xO_y composites (C), M= Al, Cr, Fe, Ce. Note: (1) $ZnAl_2O_4$, (2) $ZnCr_2O_4$, (3) $ZnFe_2O_4$, (4) $ZnTiO_3$

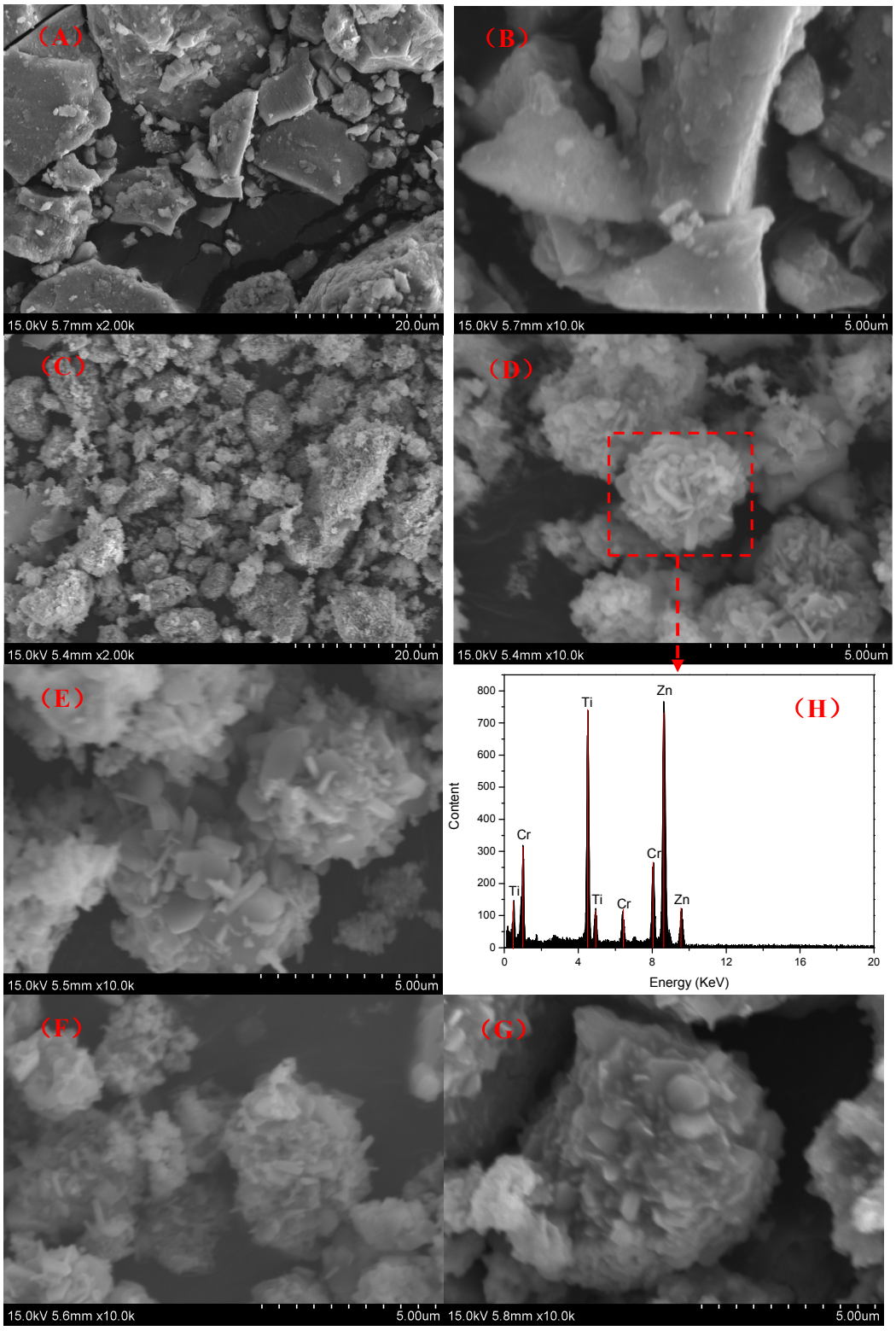

Figure 2 SEM images of samples: A, B for ZnCr–LDHs with low– and high–magnification; C, D for Ti/ZnO–Cr_2O_3 with low– and high–magnification, H is the EDS analysis of designated area; E, F, G for Ti/ZnO–Al_2O_3, Ti/ZnO–Fe_2O_3, Ti/ZnO–CeO_2 with high–magnification.

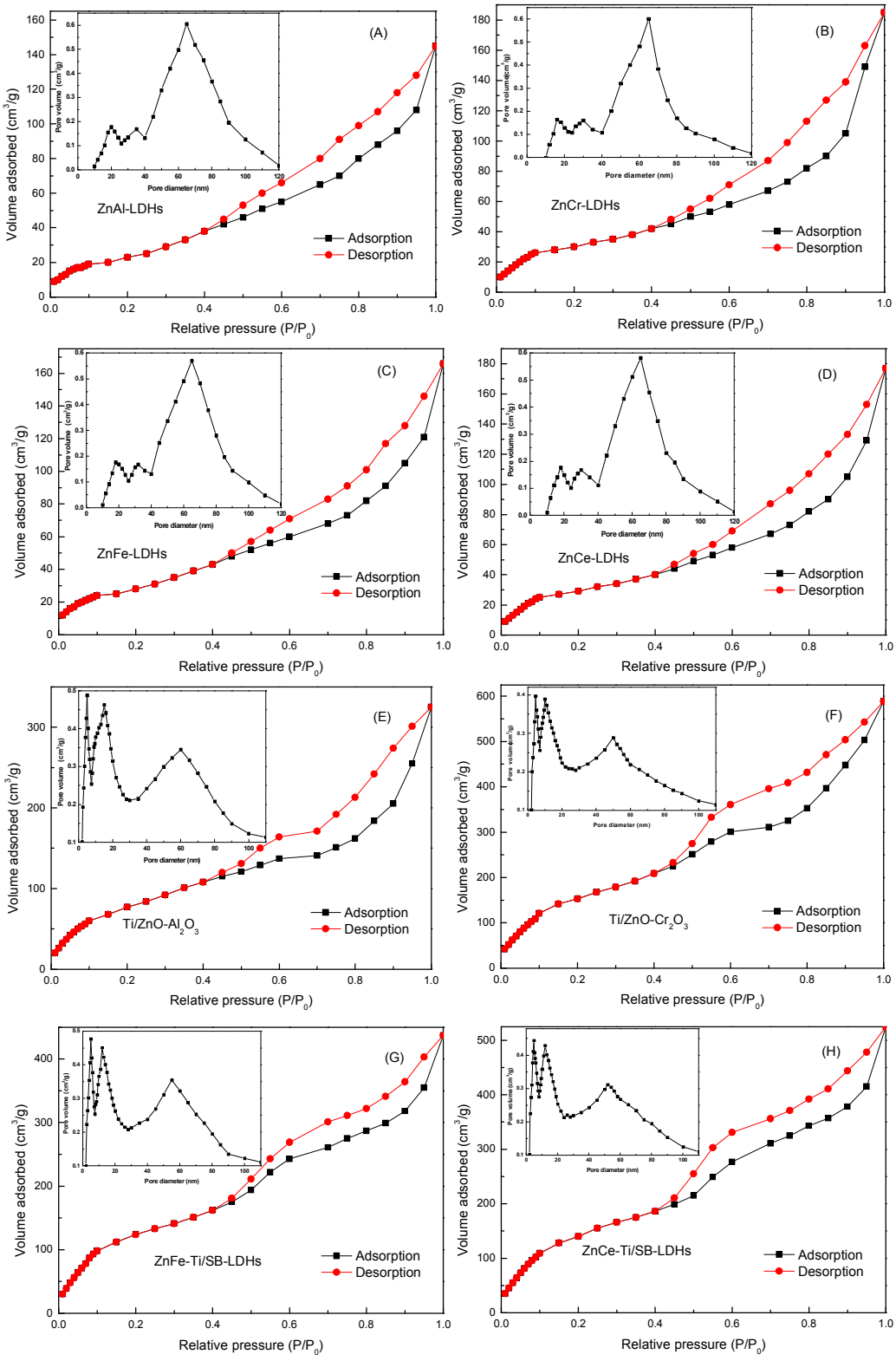

Figure 3 N_2 sorption isotherms and pore size distribution of ZnM–LDHs and Ti/ZnO–M_xO_y composites (M= Al, Cr, Fe, Ce).

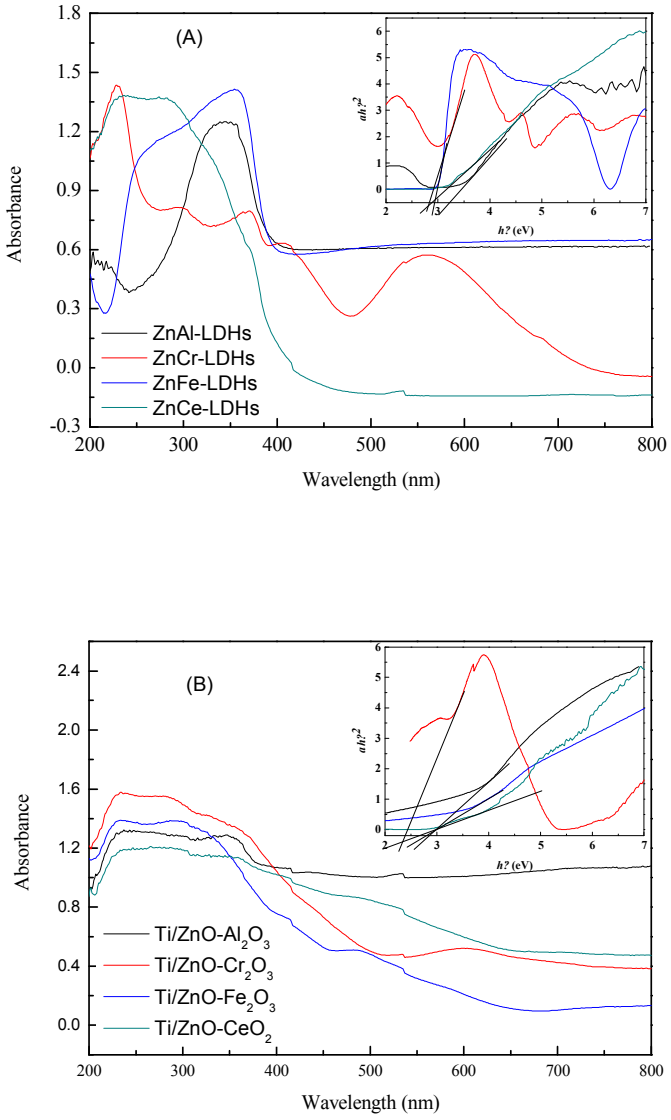

Figure 4 The UV–vis curves and plots of $(\alpha hv)^2$ *vs* *hv* for (A) ZnM–LDHs and (B) Ti/ZnO–M_xO_y composites (M=Al, Cr, Fe, Ce).

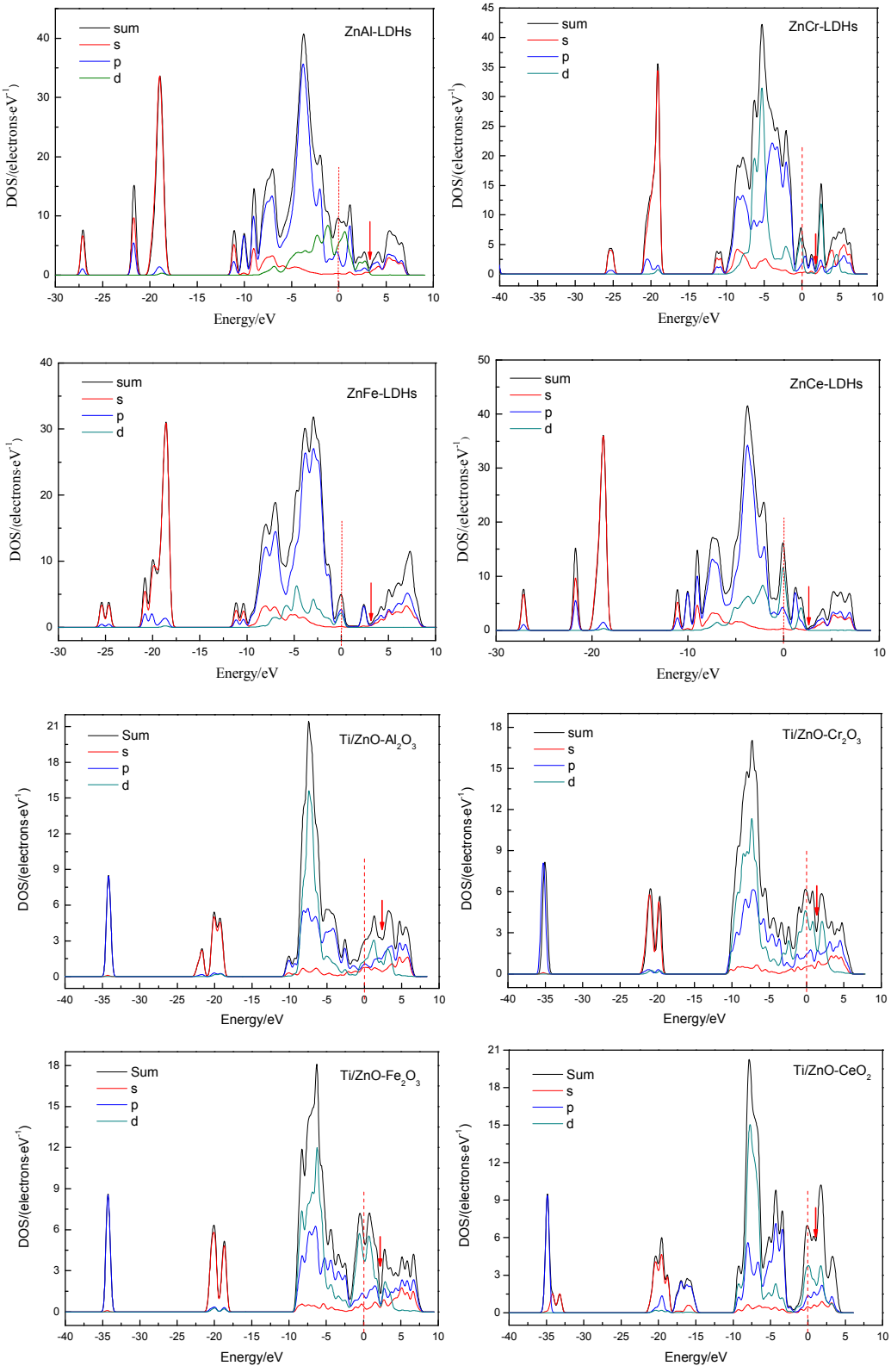

Figure 5 Total and partial electronic density of states (TDOS and PDOS) for the ZnM–LDHs and Ti/ZnO–M_xO_y composites (M=Al, Cr, Fe, Ce).

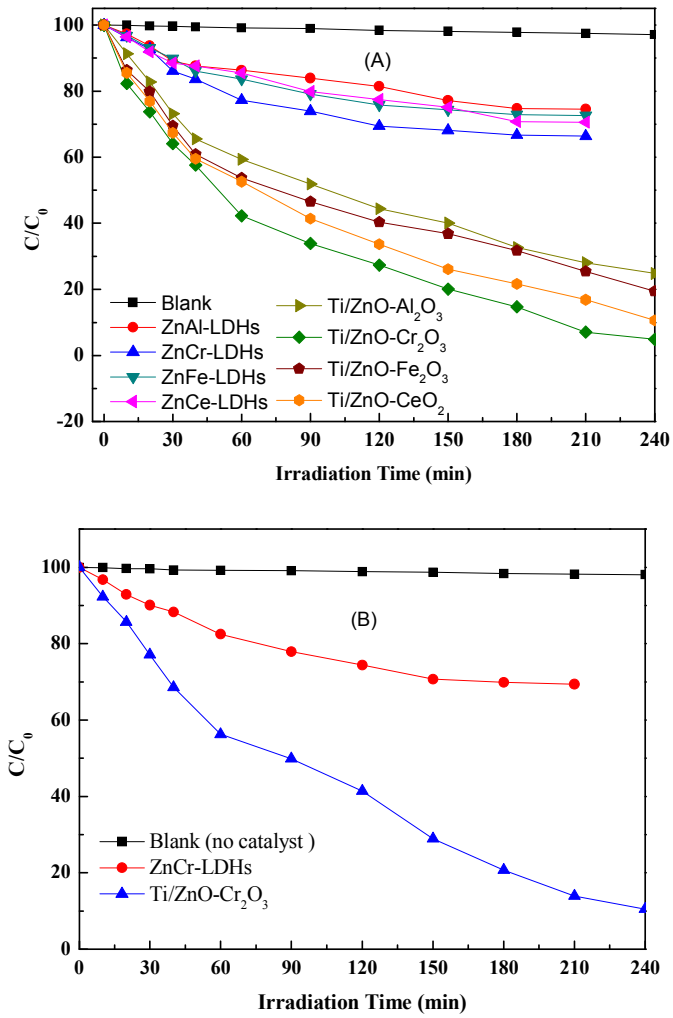

Figure 6 The photodegradation curves of HCB (A) and total organic carbon concentration (B) by samples under visible–light irradiation. Note: blank experiment means taking reaction system under vigorously stirred for 30 min to establish an adsorption/desorption equilibrium in dark before photocatalytic tests.

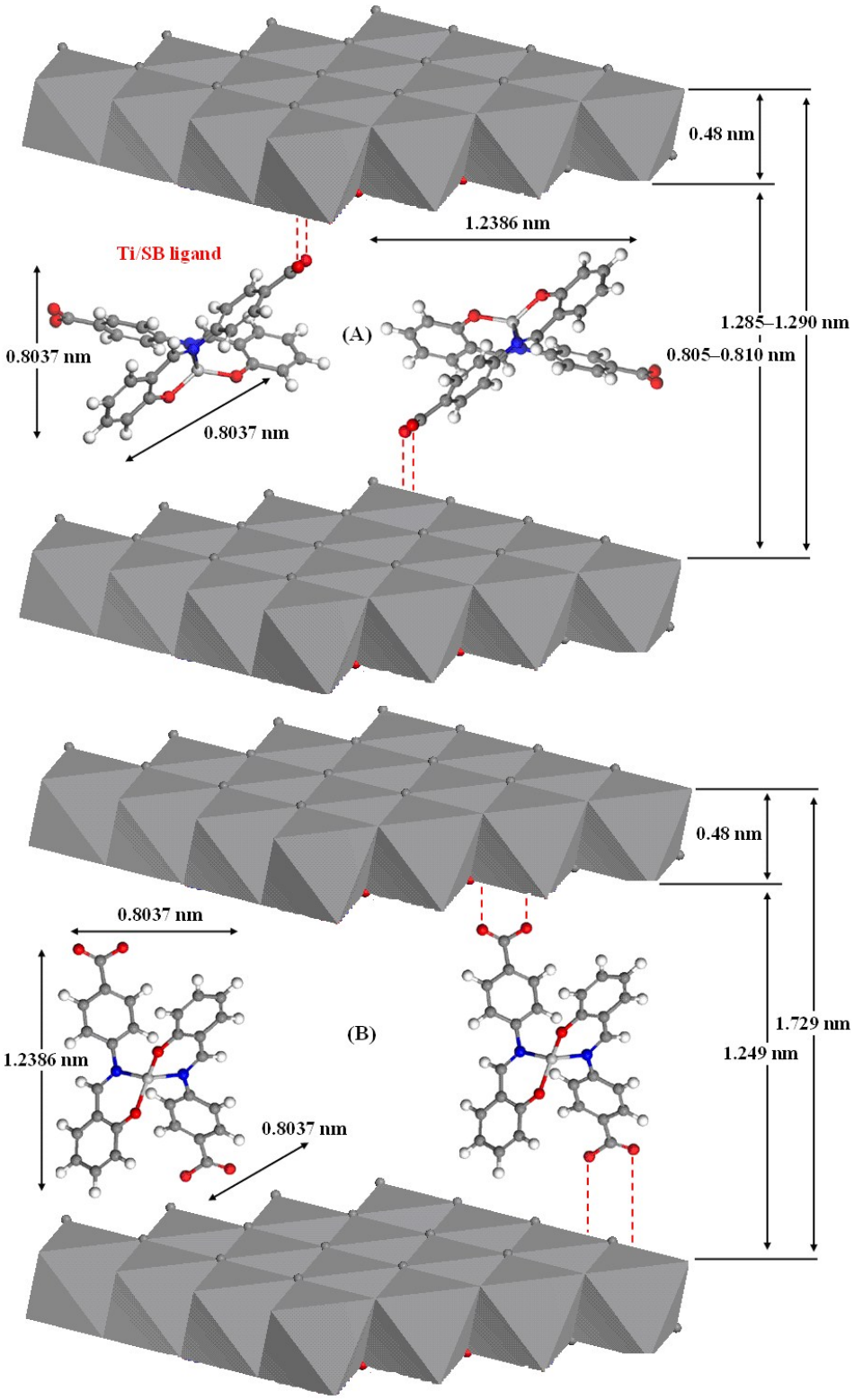

Figure 7 The schematic illustration for ZnAl–Ti/SB–LDHs and ZnFe–Ti/SB–LDHs (A), ZnCr–Ti/SB–LDHs and ZnCe–Ti/SB–LDHs (B).

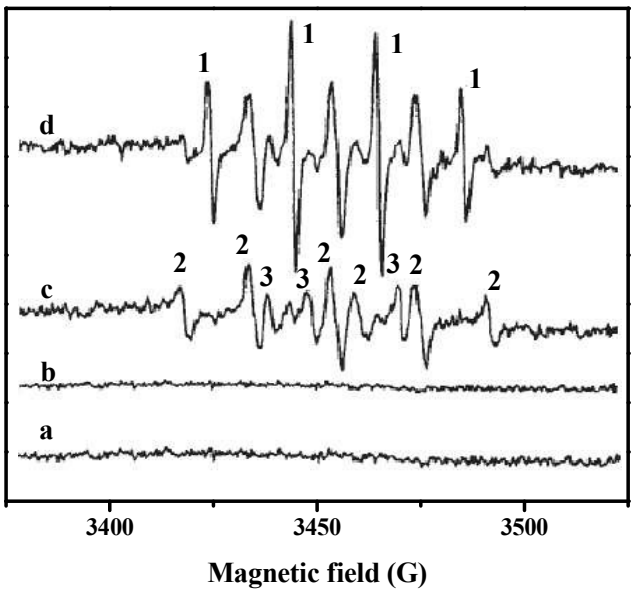

Figure 8 ESR spectrum of ZnCr–LDHs (curve *a* for dark, *c* for visible light irradiation), and Ti/ZnO–Cr_2O_3 composite (curve *b* for dark, *d* for visible light irradiation).

Note: 1. DMPO–·OH; 2. DMPO–·O_2^-; 3. DMPO–·OOH.

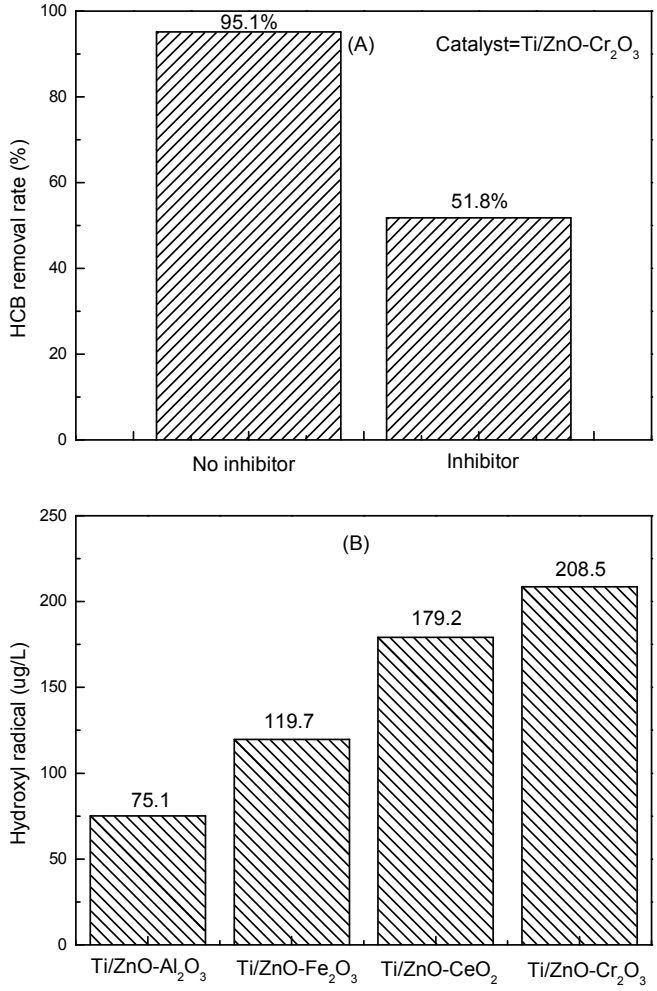

Figure 9 The HCB photodegradation contrast between inhibitor and no inhibitor (A) and the production of hydroxyl radical for different composites (B) (salicylaldehyde=2 mmol/L, t=30min).

Table 1 The chemical composition of LDHs and Ti/ZnO–M_xO_y composites.

Samples	Zn wt%	Al wt%	Cr wt%	Fe wt%	Ce wt%	Ti wt%	Chemical formula
ZnAl–LDHs	41.5	6.05	–	–	–	–	$Zn_{0.74}Al_{0.26}(OH)_2(NO_3^-)_{0.32}$ $0.39H_2O$
ZnCr–LDHs	39.2	–	11.0	–	–	–	$cZn_{0.74}Cr_{0.26}(OH)_2(NO_3^-)_{0.32}$ $0.41H_2O$
ZnFe–LDHs	38.0	–	–	12.1	–	–	$Zn_{0.73}Fe_{0.27}(OH)_2(NO_3^-)_{0.33}$ $0.43H_2O$
ZnCe–LDHs	35.1	–	–	–	22.6	–	$Zn_{0.77}Ce_{0.23}(OH)_2(NO_3^-)_{0.31}$ $0.40H_2O$
ZnAl–Ti/SB–LDHs	24.3	3.54	–	–	–	4.60	$Zn_{0.74}Al_{0.26}(OH)_2$ $((C_{14}H_{10}NO_3)_2Ti)_{0.19}$ $0.48H_2O$
ZnCr–Ti/SB–LDHs	24.5	–	6.53	–	–	4.33	$Zn_{0.75}Cr_{0.25}(OH)_2$ $((C_{14}H_{10}NO_3)_2Ti)_{0.18}$ $0.47H_2O$
ZnFe–Ti/SB–LDHs	23.4	–	–	7.07	–	4.42	$Zn_{0.74}Fe_{0.26}(OH)_2$ $((C_{14}H_{10}NO_3)_2Ti)_{0.19}$ $0.50H_2O$
ZnCe–Ti/SB–LDHs	23.4	–	–	–	15.0	3.80	$Zn_{0.77}Ce_{0.23}(OH)_2$ $((C_{14}H_{10}NO_3)_2Ti)_{0.17}$ $0.46H_2O$
Ti/ZnO–Al_2O_3	54.8	7.47	–	–	–	10.5	$(ZnO)_{3.65}(Al_2O_3)_{0.52}(TiO_2)_{0.92}$ $(ZnAl_2O_4)_{0.11}(ZnTiO_3)_{0.08}$
Ti/ZnO–Cr_2O_3	52.4	–	13.2	–	–	9.38	$(ZnO)_{3.78}(Cr_2O_3)_{0.47}(TiO_2)_{0.84}$ $(ZnCr_2O_4)_{0.18}(ZnTiO_3)_{0.16}$
Ti/ZnO–Fe_2O_3	50.3	–	–	14.1	–	10.4	$(ZnO)_{3.33}(Fe_2O_3)_{0.45}(TiO_2)_{0.90}$ $(ZnFe_2O_4)_{0.13}(ZnTiO_3)_{0.10}$
Ti/ZnO–CeO_2	41.0	–	–	–	27.9	7.58	$(ZnO)_{3.85}(CeO_2)_{1.26}(TiO_2)_{0.86}$ $(ZnTiO_3)_{0.14}$

Table 2 The band gap energy and textural properties of samples.

Catalyst	Surface area (m^2/g)	Pore volume (cm^3/g)	Pore size distribution (nm)	Eg (eV)	
				UV–vis	DFT
ZnAl–LDHs	88	0.587	20, 35, 65	3.23	2.91
ZnCr–LDHs	109	0.521	16, 30, 65	2.77	2.54
ZnFe–LDHs	95	0.559	18, 32, 65	2.88	2.79
ZnCe–LDHs	101	0.540	18, 30, 65	2.82	2.63
Ti/ZnO–Al_2O_3	155	0.471	5.0, 15, 60	2.80	2.48
Ti/ZnO–Cr_2O_3	227	0.398	4.5, 10, 52	2.40	2.25
Ti/ZnO–Fe_2O_3	178	0.462	5.0, 12, 55	2.75	2.41
Ti/ZnO–CeO_2	199	0.425	4.8, 12, 52	2.68	2.33